

H-alpha features with hot onsets. I. Ellerman bombs

R. J. Rutten

¹ Lingezicht Astrophysics, 't Oosteneind 9, 4158 CA Deil, The Netherlands

² Institute of Theoretical Astrophysics, University of Oslo, P.O. Box 1029, Blindern, N-0315 Oslo, Norway

Received May 7, 2015 / Accepted January 13, 2016

ABSTRACT

Ellerman bombs are transient brightenings of the wings of the Balmer lines that uniquely mark reconnection in the solar photosphere. They are also bright in strong Ca II and ultraviolet lines and in ultraviolet continua, but they are not visible in the optical continuum and the Na I D and Mg I b lines. These discordant visibilities invalidate all published Ellerman bomb modeling. I argue that the assumption of Saha-Boltzmann lower-level populations is informative to estimate bomb-onset opacities for these diverse diagnostics, even and especially for H α , and employ such estimates to gauge the visibilities of Ellerman bomb onsets in all of them. They constrain Ellerman bomb formation to temperatures 10 000–20 000 K and hydrogen densities around 10¹⁵ cm⁻³. Similar arguments likely hold for H α visibility in other transient phenomena with hot and dense onsets.

Key words. Sun: activity – Sun: atmosphere – Sun: magnetic fields

1. Introduction

Ellerman (1917) discovered intense short-lived brightenings of the extended wings of the Balmer H α line at 6563 Å which are called “Ellerman bombs” (henceforth EB) since McMath et al. (1960) or “moustaches” after their rediscovery by Severny (1956). The extensive EB literature was reviewed by Rutten et al. (2013). Recent studies are discussed in Vissers et al. (2015). This paper treats EB visibilities.

Below I refer frequently to a series of observational EB studies using high-quality imaging spectroscopy and polarimetry with the CRisp Imaging SpectroPolarimeter (CRISP, Scharmer et al. 2008) at the Swedish 1-m Solar Telescope (SST, Scharmer et al. 2003). Paper I (Watanabe et al. 2011) established that EBs are a purely photospheric phenomenon. Paper II (Vissers et al. 2013) added evidence that EBs mark magnetic reconnection of strong opposite-polarity field concentrations and treated their appearance in ultraviolet continuum images from the Atmospheric Imaging Assembly (AIA, Lemen et al. 2012) onboard the Solar Dynamics Observatory (SDO, Pesnell et al. 2012). Paper III (Vissers et al. 2015) presented the marked appearance of EBs in ultraviolet Si IV, C II and Mg II lines in spectra taken with the Interface Region Imaging Spectrograph (IRIS, De Pontieu et al. 2014). Paper IV (Rutten et al. 2015) confirmed Ellerman’s statement that EBs are not obvious in the optical continuum nor in the Na I D and Mg I b lines.

In summary, the visibilities of EBs are now well documented. They present a rich set of constraints with large and puzzling variety. EBs appear very bright and with extraordinary spectral extent in Balmer-line wings, also bright but less extended in the wings of Ca II H & K and Ca II 8542 Å, very bright in the IRIS C II 1334 & 1335 Å and Si IV 1394 & 1403 Å doublets, and bright and very bright in AIA’s 1700 and 1600 Å channels, respectively. However, they are transparent in the optical continuum and also absent or nearly absent in optical neutral-atom lines (Fe I, Na I, Mg I).

These diverse EB visibilities and non-visibilities invalidate the EB modeling published so far. Kitai (1983), Berlicki et al. (2010), Bello González et al. (2013) and Berlicki & Heinzel (2014) performed H α synthesis from best-fit ad-hoc perturbations of a static 1D standard model of the solar atmosphere to reproduce observed H α wing brightenings. These modeling efforts were summarized in Paper IV together with their failures: non-reproduction of the observed photospheric anchoring of EBs in internetwork lanes (Paper I), non-reproduction of EB brightening in IRIS Si IV and C II lines (Paper III), and non-reproduction of EB non-visibility in the Na I D and Mg I b lines (Paper IV).

In addition to these ad-hoc H α -synthesis attempts there have been numerical MHD simulations of EB reconnection by Archontis & Hood (2009), but without any spectral synthesis or verification, and by Nelson et al. (2013) who probably did not emulate an EB nor observed one (Paper III).

In the present paper I discuss EB visibilities assuming local thermodynamic equilibrium (LTE) for line extinctions, i.e., Saha-Boltzmann lower level populations. This assumption may seem surprising for such utterly non-equilibrium fast-changing dynamic phenomena, since EBs mark magnetic reconnection at small spatial and short temporal scales (Paper I, Paper II), including near-instantaneous heating, bi-modal jet formation (Paper I, Paper III), hot-cloud expansion (Paper III), and possibly cooling clouds in their aftermath (Paper III, Paper IV).

Assuming LTE (i.e., validity of Boltzmann and Saha partitioning over atomic levels and ionization stages) seems totally out of the question for EBs. Even the assumption of statistical equilibrium (SE, time-independent level and stage populations) seems highly questionable. This assumption is the basis for both non-LTE modeling (NLTE, meaning SE including all pertinent bound-bound and bound-free population processes) and coronal-equilibrium modeling (CE, admitting only collisional excitation and ionization and only radiative deexcitation and recombination including dielectronic), but SE is unlikely to hold in EBs. These then require non-equilibrium modeling (non-E, i.e., solving all pertinent population and radiation equations time-dependently).

My LTE approach below (Sect. 3) may seem even more surprising in view of my background (e.g., Rutten 2003, henceforth RTSA). Let me emphasize at the outset that realistic EB modeling does require 3D time-dependent non-E MHD simulation including non-E 3D spectral synthesis. The actual NLTE departures may reach 10^{10} (10 dex) or more, far beyond the 0.01–0.1 dex departures discussed in abundance analyses. However, such computations have been accomplished in full only for 1D cases, in 2D only with questionable shortcut recipes. The 3D case remains prohibitive (Carlsson & Leenaarts 2012). Leenaarts et al. (2012, 2015) therefore restricted their numerical 3D H α formation studies to a single simulation snapshot.

In this paper I first argue on the basis of published modeling that the LTE simplification can serve to gauge potential EB visibilities. The crux is to assume LTE not all the time but only during hot and dense EB onsets and only for line extinctions, not for line source functions. I then combine this onset assumption with the observed EB visibilities to define the probable EB parameter domain.

The organization of the paper is as follows. The next section gives background. It starts with basic equations and their implementation. It then treats three published solar-atmosphere models: the 1D SE static model of Avrett & Loeser (2008), the 2D time-dependent non-E MHD simulation of Leenaarts et al. (2007), and the 1D SE static model of Fontenla et al. (2009). All three were intended to mimic the solar atmosphere, but I treat them as fictitious stellar atmospheres named ALC7, HION and FCHHT-B. The HION atmosphere inspired this study. The ALC7 and FCHHT-B chromospheres supply instructive line formation demonstrations even though they are poor renderings of the actual solar chromosphere. From these examples I distill recipes for estimating line extinction (Sect. 2.5). Sect. 2.6 concludes the background part by defining observational terms to avoid confusions.

The analysis (Sect. 3) boils down to plotting and interpreting classical diagrams. Figure 4 compares LTE to CE ionization equilibria, the latter following Jordan (1969), because within the SE assumption these represent extremes. Figure 5 emulates the famous diagram¹ in Fig. 8 of Payne (1925) (first printed in Fig. 1 of Payne 1924 and redrawn in Fig. 5-6 of Novotny 1973).

Sects. 4 and 5 add a brief discussion and conclusions.

2. Background

2.1. Equations and implementation

This section specifies the basic line formation equations used to compute and interpret Figs. 1 and 3 – 5 below.

The line extinction per cm path length is given by (RTSA Eq. 9.6):

$$\alpha^l = \frac{\pi e^2}{m_e c} \frac{\lambda^2}{c} b_l \frac{n_l^{\text{LTE}}}{N_E} N_H A_E f_{lu} \varphi \left[1 - \frac{b_u}{b_l} \frac{\chi}{\varphi} e^{-hc/\lambda kT} \right], \quad (1)$$

where e is the electron charge, m_e the electron mass, c the velocity of light, λ the line wavelength, b_l the lower-level and b_u the upper-level NLTE population departure coefficient defined as $b \equiv n/n^{\text{LTE}}$, n_l^{LTE}/N_E the lower-level population density given

¹ I taught making Saha-Boltzmann graphs to hundreds of students at Utrecht and elsewhere with a lab exercise “Cecilia Payne” (available on my website). It uses a fictitious and unpronounceable didactic element called “Schadeenium” after Utrecht astrophysicist Aert Schadee (1936–1999), who invented it for teaching in the 1970s.

by the Saha and Boltzmann laws as fraction of the total element density N_E , N_H the total hydrogen density, A_E the elemental abundance, N_E/N_H , f_{lu} the lower-to-upper oscillator strength, φ the area-normalized extinction profile in wavelength, χ the induced-emission profile, h the Planck constant, k the Boltzmann constant, and T the temperature. The profiles φ and χ differ in the case of partial frequency redistribution (PRD) but are equal for complete redistribution (CRD).

The line source function is given by:

$$S^l = (1 - \varepsilon - \eta) J + \varepsilon B + \eta S^D, \quad (2)$$

where ε is the photon destruction probability (the fraction of photoexcitations followed by direct collisional upper-to-lower deexcitation), η the photon conversion probability (the fraction of photoexcitations followed by detour upper-to-lower paths), J the angle-averaged intensity (profile-averaged \bar{J} for CRD or a wavelength-dependent mix of the monochromatic J_λ for PRD), B the Planck function for the local temperature, and S^D a formal source function which collectively describes all multi-level upper-to-lower detour chains (sometimes written as $B(T^D)$ with T^D a formal detour temperature as in Eqs. 8.5–8.8² of Jefferies 1968). Eq. 2 is the multi-level extension of the two-level version including scattering (Eq. 10 of Hummer & Rybicki 1967, Eq. 1.95 of Rybicki & Lightman 1979, Eqs. 3.94 and 3.105 of RTSA, Eq. 14.34 of Hubeny & Mihalas 2014) and follows from that following Sect. 8.1 of Jefferies (1968).

For the Wien approximation with $hc/\lambda kT > 1$ the simple expressions hold:

$$\alpha^l \approx b_l \alpha^{\text{LTE}}, \quad (3)$$

$$S^l \approx (b_u/b_l) B. \quad (4)$$

This is the case for all diagnostics treated here (Ca II 8542 Å reaches $\lambda kT = hc$ at 16 800 K, H α at 21 900 K). These equations illustrate that extinction NLTE ($b_l \neq 1$) and source function NLTE ($b_u/b_l \neq 1$) are different entities, as are extinction and source function themselves.

The emergent intensity which conveys our telescopic diagnostics is usually well approximated by the Eddington-Barbier estimate $I \approx S(\tau = 1)$ for optically thick formation with τ the optical depth along the line of sight. For non-irradiated optically thin slabs it is $I \approx jD = \tau S$, with emissivity $j = \alpha S$ per cm, geometrical thickness D , and optical thickness τ .

In the thick case extinction NLTE affects only the representative $\tau = 1$ sampling depth (Eq. 3), whereas source function NLTE affects the intensity directly. In the thin case both extinction and source function NLTE affect the intensity directly by together setting the emissivity.

NLTE SE spectrum synthesis codes, such as the workhorse RH code of Uitenbroek (2001), solve the coupled population and radiation equations for all transitions and locations pertinent to selected lines, or even the whole spectrum. I use RH in the latter mode in Sect. 2.2 below.

For the simpler LTE extinction evaluations I updated IDL codes to compute ionization and molecule mixes and partial pressures for given elemental composition that were developed by J. Sánchez Almeida (1992, 1997) and are partly based on Wittmann (1974) following Mihalas (1967). I found them in the [github LTE repository](#) of A. Asensio Ramos and extended them with data and routines in the SolarSoft CHIANTI package (e.g., Dere et al. 1997, Landi et al. 2013). My codes are available under IDL on [my website](#).

² Correction: delete the minus in the second version of Eq. 8.8.

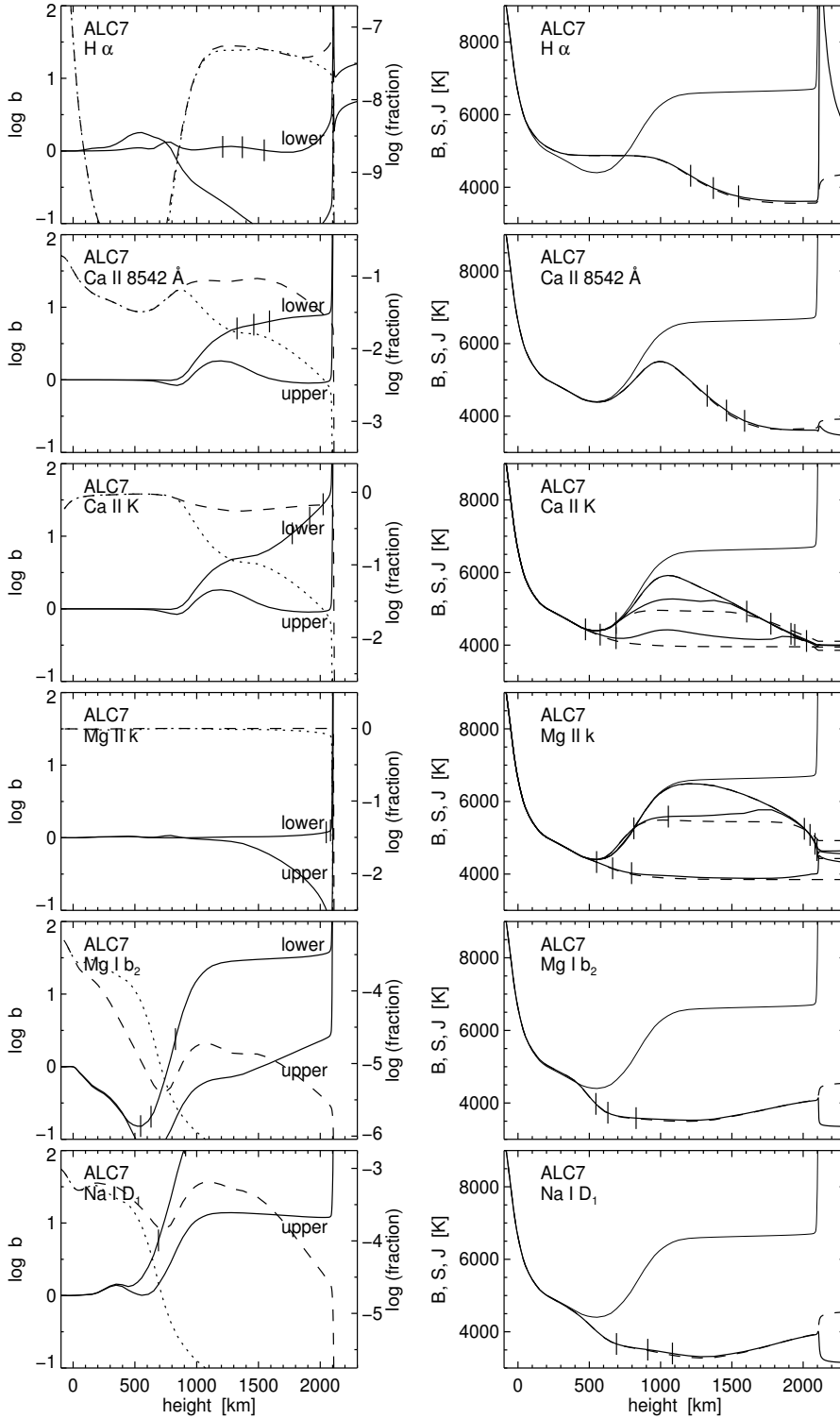


Fig. 1. SE formation of EB diagnostics in the ALC7 model atmosphere of [Avrett & Loeser \(2008\)](#) computed with the RH code of [Uitenbroek \(2001\)](#).

Left, solid: logarithmic NLTE population departure coefficients $b \equiv n/n^{\text{LTE}}$ as function of height, respectively b_l for the lower level and b_u for the upper level of the line identified in each panel.

Left, dashed: logarithmic lower-level populations normalized by the total element density (axis scales to the right).

Left, dotted: the same fractional population in LTE.

Right: Planck function B_λ (*thin solid*, the same in all panels), angle-averaged intensity \bar{J} or J_λ (*dashed*), line source function S_λ (*solid*). These quantities are plotted as representative temperatures to avoid the Wien sensitivity of the Planck function and so obtain directly comparable scales. For PRD lines (Ca II K and Mg II k) S_λ and J_λ are shown for line center and the emergent-profile peaks and dips. The three vertical ticks define the heights where total optical depth $\tau_\lambda = 3, 1, 0.3$, respectively (in the left-hand column only for line center on the b_l curve). The $S < B$ splits correspond to the $b_u < b_l$ divergences at left.

Remarkable: at left the very deep dip in the dashed $H\alpha$ population curve, the relative flatness of the Ca II 8542 Å and Ca II K population curves, the utter flatness of the Mg II k population curve, and the large chromospheric overpopulations from photon suction for the Mg I b_2 and Na I D_1 lower levels. At right the discordantly high value of $S \approx J$ for $H\alpha$ across the temperature minimum from backscattering and the overall similarity of the scattering $S \approx J$ declines of all lines, including independently scattering PRD wings.

2.2. ALC7: EB diagnostics in 1D SE modeling

This section presents and discusses the formation of EB diagnostics in quiescent conditions in order to establish their normal behavior.

Figure 1 presents EB diagnostics assuming SE and E.H. Avrett’s latest empirical static 1D model ([Avrett & Loeser 2008](#)). Below I question the validity of such plane-parallel models, but they do remain exemplary for demonstrating fully understandable solar-like line formation, in this case in the computational atmosphere “ALC7”.

Figure 1 shows extinction parameters at left, source function parameters at right. They were computed with the 1D RH version of [Uitenbroek \(2001\)](#) including NLTE line blanketing with the full compilation of [Kurucz \(2009\)](#). PRD was adopted for Ca II K and Mg II k; CRD for the others. The IRIS C II and Si IV lines were excluded because they form in the ALC7 TR and pose numerical difficulties.

In the left-hand column the divergences between the dashed and dotted fractional population curves correspond to the departure of $\log b_l$ from zero. All plots show increasing $b_u < b_l$ di-

vergence with height due to photon losses. Equation 4 implies that these divergences translate into equal divergences between S and B , but the equivalent temperature representation used at right produces larger divergence at longer wavelength for given b_u/b_l .

$H\alpha$ (top panels of Fig. 1) has discordant formation across the upper ALC7 photosphere because this is transparent in this high-excitation line (dashed curve in the first panel). The radiation field there builds up from backscattering from the opaque overlying ALC7 chromosphere (Rutten & Uitenbroek 2012). The lower-level population, hence the $H\alpha$ line extinction, nearly equals the Saha-Boltzmann value up to the ALC7 TR thanks to the huge $\text{Ly}\alpha$ opacity producing $S^I \approx J \approx B$ in this line, with small wiggles from radiative $\text{Ly}\alpha$ smoothing (Sect. 2.4).

The $H\alpha$ source function (second panel) behaves like a standard scattering one, i.e., domination of the first two terms in Eq. 2 that together cause a scattering decline in b_u/b_l . $H\alpha$ has often been called “photoelectric” following Thomas (1957), meaning dominance of the third term in Eq. 2 over the second, but across the ALC7 chromosphere it is simply a resonance-scattering line with a source function decline like all others in Fig. 1

Since the ALC7 chromosphere is near-isothermal there is good resemblance to the classic demonstration of two-level scattering by Avrett (1965), except that ε is not constant.

The outward S decline from such scattering (“ $\sqrt{\varepsilon}$ law”) causes a dark line core which is often called “self-absorption” in ultraviolet spectroscopy.

In the ALC7 atmosphere the $H\alpha$ core forms halfway the chromosphere, but most escaping photons actually originated in the deep ALC7 photosphere where ε reaches unity. For $H\alpha$ the ALC7 chromosphere is only a scattering re-director. If it were absent the emergent $H\alpha$ profile would remain the same, originating in a similar scattering decline within the photosphere.

In actual solar $H\alpha$ images such scattering (but 3D) obliterates the granulation imprint although this has larger intrinsic contrast than chromospheric fine structure, making the latter visible. Where the chromospheric slab has larger density the $\tau = 1$ location moves outward along the scattering decline, making $H\alpha$ core darkness primarily a density diagnostic (Leenaarts et al. 2012).

$\text{Ca II } 8542 \text{ \AA}$ (second row) forms at about the same height as $H\alpha$ in ALC7, but has a better-behaved source function that follows the temperature until it drops down from scattering. The b_l curve in the lefthand panel shows substantial increase from photon losses in the Ca II infrared lines. The initial dip in the population curve follows the temperature through the Boltzmann sensitivity.

Ca II K behaves very similar to $\text{Ca II } 8542 \text{ \AA}$, but its core forms higher and PRD applies, shown by sampling S and J at the K_3 , K_2 and K_1 wavelengths (cf. Shine et al. 1975). The b_l curve first rises from photon losses in the Ca II infrared lines that are shared through collisional lower-level coupling, then from photon losses in H & K. They offset the Ca II depletion by ionization that would occur in LTE (dotted curve).

Mg II k behaves much as Ca II K , but the 18 times larger Mg abundance makes it form in the ALC7 TR. Its PRD wings form across the ALC7 chromosphere. The higher ionization energy (15.0 eV instead of 11.9 eV) makes Mg II fully dominant throughout the ALC7 chromosphere (dashed curve in the lefthand panel), resulting in pure LTE extinction and textbook decline of the b_u curve.

$\text{Mg I } b_2$ and $\text{Na I } D_1$ (last rows) have their $\tau = 1$ escape levels in the onset of the ALC7 chromosphere, but the escaping pho-

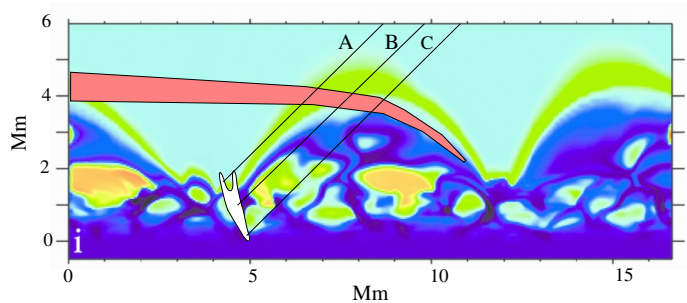


Fig. 2. Schematic EB in the HION atmosphere. A sketched EB (white, near $x = 5$) is superimposed on the last panel of Fig. 1 of Leenaarts et al. (2007) in which the black–blue–green–orange color coding quantifies NLTE overpopulation of the $\text{H I } n=2$ level ranging from 1 to 10^{14} . The superimposed pink arch represents a schematic $H\alpha$ fibril. Slanted lines of sight ($\mu = 0.71$) to the top, middle, and bottom of the EB are marked A, B, and C.

tons originate so deep that the line core intensity does not sense the ALC7 chromosphere. These lines have large extinction increase over LTE from minority-stage photon suction (Bruels et al. 1992). Below that, Mg I shows a steep departure-coefficient decline from overionization by ultraviolet radiation from below (Rutten & Uitenbroek 2012).

In summary, Fig. 1 shows that LTE extinction is a reasonable assumption for these EB diagnostics throughout the ALC7 chromosphere. In particular, it is valid for the Balmer lines and the Balmer continuum and for Mg II k , whereas it even represents considerable underestimation for the Ca II lines and $\text{Na I } D_1$. It is an overestimation only for $\text{Mg I } b_2$.

EB-like hot and dense features embedded in such an atmosphere will have larger collisional coupling, especially when hydrogen ionization boosts the electron density and ε , and be yet closer to LTE.

2.3. HION: $H\alpha$ extinction boost to past hot LTE

This section presents the motivation for assuming LTE extinction in hot onsets of dynamical phenomena.

This assumption was inspired by the numerical non-E MHD simulation of Leenaarts et al. (2007). It did not address EBs but a vertical plane containing two opposite-polarity strong-field concentrations resembling solar network with less magnetic inter-network in between. Its theme was non-E modeling by permitting and evaluating time-dependent hydrogen ionization and recombination. By being 2D and MHD it represented a sequel to the seminal 1D non-E HD simulation of Carlsson & Stein (2002) in which the physics of non-E hydrogen population processes was analyzed for acoustic shocks in the lower solar atmosphere.

Below I refer so much to this simulation that I treat it as the atmosphere of a hypothetical star called “HION” (for H I ionization). Its atmosphere exists only computationally but yet has solar-like properties.

In the HION atmosphere shocks occur copiously as field-guided ones producing dynamic fibrils near the magnetic concentrations and as less field-restricted ones in the quieter inter-network that resemble the acoustic 1D shocks of Carlsson & Stein (1997).

Figure 2 superimposes a sketch of an EB based on the SST images in Papers I–IV on a snapshot of the HION atmosphere. I use the latter as a scenic illustration of how the actual shock-ridden lower solar atmosphere around an EB may look like. The two opposite-polarity field concentrations at $x = 4$ and $x = 12 \text{ Mm}$

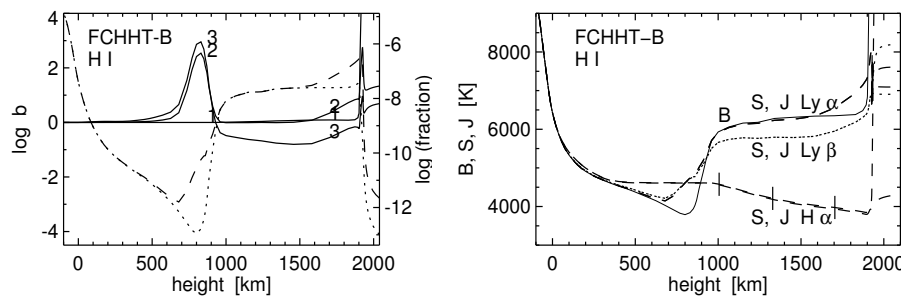


Fig. 3. SE formation of H α , Ly α , and Ly β in the FCHHT-B atmosphere of Fontenla et al. (2009) in the format of Fig. 1, using RH results from Rutten & Uitenbroek (2012). The lefthand panel shows NLTE departure coefficients b for hydrogen levels $n = 1, 2, 3$. The dashed and dotted NLTE and LTE fractional population curves are for $n = 2$. The righthand panel shows the corresponding line source functions.

closely resemble the actual kilogauss magnetic concentrations that constitute solar network. Besides them and elsewhere finely-structured thin shocks (black to dark blue) run up and push the transition region (TR, onset of the light-blue area) to large heights, of order 3 Mm. Large cool clouds appear behind the shocks (green to orange). This scene is very dynamic: the HION TR in HION dances up and down over 2–4 Mm height in inter-network and over 1.5–2.5 Mm in and near the field concentrations.

What does this HION scene have to do with assuming LTE? (It actually depicts H α NLTE b_i departures of twelve orders of magnitude in the orange clouds!) The essential non-E hydrogen-ionization physics is that collisional transitions between H I $n = 1$ and $n = 2$ are so scarce in cool post-shock gas that there hydrogen ionization/recombination balancing is slow (Kneer 1980; Carlsson & Stein 2002), leaving the ion state and with it the top of the hydrogen atom highly overpopulated with respect to Saha-Boltzmann partitioning during the 3–5 minute cool intermezzo until the next shock passes.

The shocked HION atmosphere is sampled in Fig. 2 of Leenaarts et al. (2007) with the bottom panels showing the H I $n = 2$ population governing the extinction of H α (Eq. 1). The first key point is that it reaches the momentary LTE value in shocks. This results from high temperature (about 7000 K) and large electron density increase from hydrogen ionization (above 1 percent), to values $10^{10} - 10^{11} \text{ cm}^{-3}$, together boosting ε for Ly α sufficiently to couple $n = 2$ to the ground state within the shocks. The second key point is that in between successive shocks the $n = 2$ population remains at or near this high level, even while the temperature drops thousands of degrees, because the top of the hydrogen atom is decoupled from the ground state during the retarded recombination.

Thus, both the H α and Balmer-continuum opacities are near-LTE in the shocks and remain at these high values between them. The gigantic overpopulations indicated by the orange clouds in Fig. 2 and the corresponding large separations between the thick and thin curves in the bottom panels of Fig. 2 of Leenaarts et al. (2007) simply mean that the actual $n = 2$ population doesn't track the cool intermezzi.

2.4. FCHHT-B: H α extinction boost to nearby hot LTE

This section addresses the effect of Ly α scattering near hot features.

Inter-shock temporal constancy of the $n = 2$ population also implies constancy of the Ly α source function which has $S \approx J \approx b_2 B(T)$ where hydrogen is predominantly neutral (Eqs. 2 and 4) which it remains even in the HION shocks. Leenaarts et al. (2007) did not admit Ly α or other Lyman radiation in HION, but it is interesting to note that, in addition to the temporal H α extinction smoothing to the hottest preceding instances in the near past due to slow recombination settling, there is also spatial

H α extinction smoothing to nearby hot instances. This is due to Ly α resonant scattering. I illustrate it in Fig. 3 using the FCHHT-B atmosphere of Fontenla et al. (2009).

The FCHHT-B atmosphere is similar in construction and properties to the ALC7 atmosphere. The main difference is that ALC7 obtains chromospheric extent from adding turbulent pressure constrained by observed non-thermal line widths while FCHHT-B obtains extent from best-fit manipulation of the local gravity. The FCHHT-B atmosphere has a low high-lying temperature minimum adjacent to an abrupt rise to a near-isothermal chromosphere (B curve in Fig. 3) intended to reproduce dark infrared CO-line cores.

I use this sudden rise as emulating a hot feature embedded in a cool atmosphere. The downward radiation from this hot edge may be seen as representing how a cylindrical hot EB irradiates cool gas around it. The large b_2 and b_3 peaks in Fig. 3 arise from downward Lyman-line scattering from the overlying chromosphere. Even at the very large optical depths which the Lyman lines reach there, their local scattering diffuses some of their intense chromospheric $J \approx B$ radiation into the cool underlying FCHHT-B layers. The Ly α irradiation boosts the $n = 2$ population and with it the H α extinction by a factor 400 at 100 km below the edge.

Ly β has a similar off-edge $S \approx J$ scattering halo as Ly α . Over $h = 1000 - 1500 \text{ km}$ the Ly α radiation confinement causes $b_2 \approx b_1 \approx 1$, so there Ly β has the same degree of source function NLTE as H α since they share $n = 3$ as their upper level (Eq. 4) and its depopulation by H α photon losses. Their S divergence from B at right differs through the representation as formal temperatures (which removes Planck function sensitivity to wavelength).

2.5. Recipes for H α extinction in EB onsets

I now apply the above to EB onsets. The upshot from Sects. 2.3 and 2.4 is that for hot dense instances in the low solar atmosphere one may: (1) assume Saha-Boltzmann lower-level population for the extinction coefficient of H α , (2) apply such boosting also as an opacity halo to cooler surrounding gas, and (3) maintain it during cooler subsequent episodes. These are the recipes applied in this paper.

Similar to the shocks pervading the HION atmosphere for which these recipes hold, EBs are momentary heating events in the low atmosphere but yet deeper, hotter and denser. I therefore suggest that the LTE recipes also apply to the hydrogen $n = 2$ population in EBs. They then hold for both H α extinction and Balmer-continuum extinction.

Do the recipes apply also to other EB diagnostics? This question is twofold: is Saha-Boltzmann population partitioning a good approximation for their extinction at hot moments at high density, and do they possess a memory for such momentarily high extinction as the Balmer lines and continuum have?

In contrast to $H\alpha$, most other EB diagnostics are ground-state resonance lines and have extinction near or at the LTE value if the pertinent ionization stage is the dominant one. For them, in particular Si IV, the question is whether Saha applies in photospheric-density gas heated to high temperature.

The second recipe issue is the presence of a memory for previous hot-feature extinction due to retarded recombination. This cannot be illustrated with static modeling. However, the H I example shows that it occurs when there is a large initial jump in the term structure of the lower stage (Carlsson & Stein 2002). He I is an obvious candidate (Golding et al. 2014), but unfortunately there are no reports of EB visibility in He I D₃ or 10 830 Å. The Na I D, Mg I b, Ca II and Mg II lines will be much less retarded (cf. Wedemeyer-Böhm & Carlsson 2011; Leenaarts et al. 2013). However, retarded recombination may well apply to C II 1334 & 1335 Å and Si IV 1394 & 1403 Å because their preceding ions have large initial jumps: C I has a 13 eV gap between low and high levels, the Si III resonance lines are like Ly α near 1200 Å. These large steps slow down recombination to the lower stage when that becomes dominant in cool gas, just as for H I in HION post-shock gas.

2.6. Terminology

This section defines observational nomenclature used in the analysis in Sect. 3.

EB, MC, FAF, IB. For clarity I list and define various EB-related observed phenomena here.

Ellerman bombs (EB) adhere to the definition by Ellerman (1917): sudden intense brightenings of the extended $H\alpha$ wings (“moustaches”) that occur exclusively in complex bipolar active regions and have the diverse visibilities described in Sect. 1.

Magnetic concentrations (MC) denote the kilogauss strong-field elements that make up solar network. They are best known as faculae or G-band bright points, but also appear as bright points in the 1700 Å continuum and especially in the blue wing of $H\alpha$ (Leenaarts et al. 2006). The latter property has caused frequent confusion with EBs (Rutten et al. 2013). Paper I showed that at high resolution upright flame morphology in limbward viewing is a distinctive EB characteristic. It was used in Paper II to establish EB brightness criteria, but these may fail close to disk center (Paper III) where differentiation with the MCs that produce EBs (as in the serpentine U-loop pull-up scenario of EB formation of e.g., Bernasconi et al. 2002, Pariat et al. 2004, Isobe et al. 2007, Archontis & Hood 2009, Pariat et al. 2009) is less easy, as already pointed out by Ellerman (1917) and later by Bruzek & Durrant (1977).

With “FAF” I denote small sudden brightenings in AIA 1600 Å images with filamentary morphology. Similarly to EBs they appear as sudden brightenings in complex active regions, but they are elongated, change faster, and show rapid apparent motion. They seem to start as EB-like reconnection events but then break through the chromospheric canopy and affect the higher atmosphere (Paper III). Pariat et al. (2009) noted them in 1600 Å images from TRACE, called them “transient loops”, and reported them as a new phenomenon – but probably $H\alpha$ -core “microflares” (e.g., Shimizu et al. 2002) describe similar outbursts. In Rutten et al. (2013) we noted them as “small flaring arch filaments and microflares” and abbreviated this to FAF = “flaring arch filament” in Paper III, but a better name is “flaring active-region fibril” to avoid confusion with the larger and sta-

bler structures making up “arch filament systems” in emerging active regions.

IRIS bombs (IB) are short-lived small-scale active-region brightenings that show very bright IRIS C II and Si IV lines with very broad doubly peaked profiles and superimposed absorption blends indicating cool overlying gas. In their discovery paper Peter et al. (2014) suggested that these are pockets of hot gas in the upper photosphere and may correspond to EBs in $H\alpha$. In Paper III we found that they are more likely FAFs while EBs may also show IB signatures in their aftermaths.

Photosphere, chromosphere, clapotisphere. Paper I concluded that EBs are a photospheric phenomenon, but also that they reach up to one Mm or more. A one-Mm tall feature embedded in the ALC7 atmosphere would have its top in the ALC7 chromosphere; that part would then be called chromospheric. However, we designated EBs instead as fully non-chromospheric, hence implicitly photospheric, because even their tops always remain shielded by the fibril canopy observed in $H\alpha$ line center in active regions. What we meant is that EBs are embedded in cool gas with upper-photosphere temperatures, as present between shocks in the internetwork areas of the HION atmosphere in Fig. 2 where it reaches 3 Mm height, higher than EBs.

However, recently Ph. Judge (private communication) insisted that one should restrict “photosphere” to its original meaning: the domain where the bulk of the solar radiation flux escapes. I follow his admonishment here and restrict “photosphere” to this thin shell which reaches no higher than about 400 km above $\tau_{5000} = 1$. Its upper layers are similar in the ALC7, HION and FCHHT-B atmospheres, with a temperature decline that is also closely the same in LTE radiative-equilibrium models. The reason is that this is the most homogeneous part of the solar internetwork atmosphere, above the granulation and below shock formation and not too magnetized; linear undulations of the acoustic p -mode pattern and internal gravity waves represent its major perturbations. The visible continuum escape is described fairly well by LTE as a small leak from a large thermal pool. Theoretical radiative-equilibrium modeling and empirical 1D static modeling apply best to the upper photosphere.

The name “chromosphere” was given by Lockyer (1868) to the pink shell he saw spectroscopically (literally) around the sun, with the beautiful color due to emission in $H\alpha$, $H\beta$, and He I D₃. It then became the name of what causes the flash spectrum (Athay & Thomas 1961), but in the past decades it became synonymous with the raised temperature plateau over $h \approx 500 - 2000$ km in Avrett-style standard models as ALC7.

I prefer to return to Lockyer’s naming and therefore define as on-disk chromosphere what one observes in $H\alpha$. In active regions this is a dense canopy of long opaque fibrils. I sketched one as example in Fig. 2 because HION does not contain such fibrils (an issue addressed in the next paper in this series). Note that the green arches in Fig. 2, which resulted from photon suction by $H\alpha$ where hydrogen ionizes, are artifacts because the HION computation did not include photon losses in the Lyman lines. In HION the H I $n=2$ level therefore acted effectively as ground state for the H I atom top.

With these definitions a third name is needed for shocked cool gas in high-reaching sub-canopy domains in solar internetwork areas and also present in HION internetwork (Fig. 2). I once again use “clapotisphere” (Rutten 1995).

Thus, a major difference between the ALC7 and HION atmospheres is that ALC7 possesses a static 1D isothermal chromo-

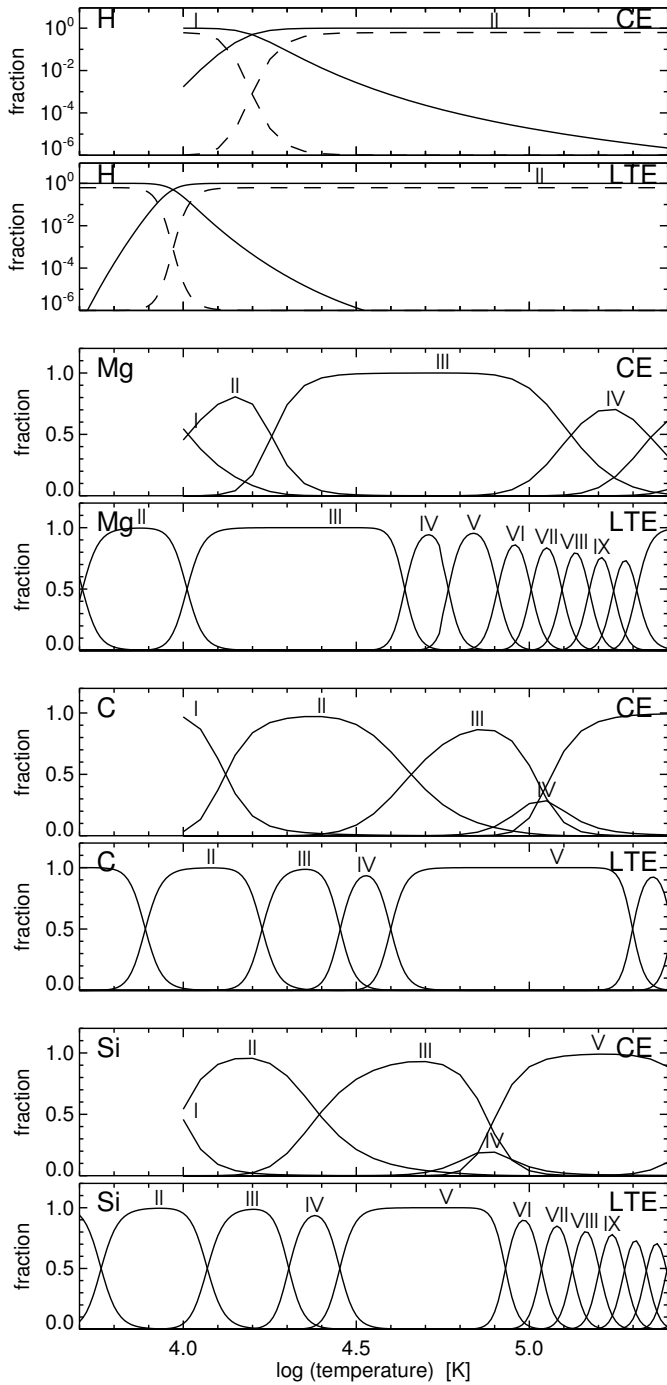


Fig. 4. CE/LTE ionization-stage population comparisons for H, Mg, C, and Si. *Upper panel of each pair:* CE distribution with temperature (CHIANTI gives no values below 10 000 K). *Lower panel of each pair:* LTE distribution with temperature for fixed electron density $N_e = 10^{14} \text{ cm}^{-3}$. For 10 times lower N_e the LTE curve patterns remain similar but the peaks shift leftward over about -0.05 in $\log(T)$ and become narrower. The first pair for hydrogen has logarithmic y -axes; the dashed curves are on the linear scales of the other panels. *Remarkable:* the substantial leftward CE to LTE shifts and the wide presences of Mg III, C V, and Si V.

sphere, HION a highly dynamic low-lying 2D network chromosphere made up of dynamic fibrils and a highly dynamic high-reaching 2D internetwork clapotisphere. This difference is enormous.

In my opinion HION comes much closer to the actual Sun even while it is only 2D and has no internetwork-covering H α fibrils. I regard the temperature stratification of ALC7-like “standard” chromospheres, for all their phenomenal didactic value, as artifacts from unrealistic static modeling. They do not describe a mean over actual temperature fluctuations because their construction through ultraviolet spectrum fitting suffers from non-linear Wien temperature sensitivity and therefore favors shocks (Fig. 4 of [Carlsson & Stein 1994](#).) Indeed, the ALC7 chromosphere has similar temperature, ionization and electron density as the HION shocks.

Worse, while every solar-atmosphere column must have a minimum temperature and a steep rise to the corona somewhere, the HION atmosphere suggests that their heights fluctuate so wildly that the static-modeling notions of “the temperature minimum” and “the transition region” are useless.

3. Analysis

3.1. LTE–CE comparisons

Figure 4 compares the fractional populations of ionization stages of H, Mg, C and Si between CE (upper panels per pair) and LTE (lower panels).

The upper panels are from CHIANTI and represent “Carole Jordan” diagrams following [Jordan \(1969\)](#) whose landmark Fig. 3 represents the solar-corona counterpart to Payne’s stellar-photosphere population distributions.

The lower panels of Fig. 4 are not strictly “Cecilia Payne” diagrams because they do not include Boltzmann excitation for particular lines but show only the distribution over successive ionization stages defined by the Saha equation. They are also based on CHIANTI data (ionization energies and term structures defining partition functions). The large electron density corresponds to full hydrogen ionization of ALC7 gas at $h = 850 \text{ km}$.

These extreme assumptions bracket the temperature regime in which the EB diagnostics form. Of course neither is likely valid, but here I suggest that EB onset visibilities, even in the IRIS lines, behave more as the lower LTE panel than the upper CE panel per pair.

The peak widths are defined by the ionization energies and are exceptionally large for the closed-shell ions Mg III, C V, and Si V, and of course for H II which suffers no competition from higher stages.

The hydrogen curves (first pair of panels) are plotted on logarithmic scales in view of the enormous hydrogen abundance: even at only $N_{\text{H I}}/N_{\text{total}} = 10^{-5}$ neutral hydrogen still competes with the dominant stages of the most abundant metals. For CE such presence extends as high as 100 000 K. For LTE the break-even ionization point shifts below 10 000 K.

The next pair (Mg) shows that due to the similarity of the Mg II and H I ionization energies (15.0 and 13.6 eV, respectively) the Mg II to Mg III transition occurs very similar to H I to H II ionization. Hence, the resonance Mg II h & k and H I Lyman lines will have similar presence apart from the $2.5 \cdot 10^4$ extinction ratio per given feature (abundance ratio), unless they also differ in being closer to the LTE limit or to the CE limit or in departure from SE.

The third and fourth pairs are for C and Si. They show similar patterns, with wide peaks for the first and especially the fourth ions. In CE the Si IV presence peaks with relatively low amplitude at $\log(T) \approx 4.9$ ($T \approx 80\,000 \text{ K}$) as quoted by [Peter et al. \(2014\)](#), but in LTE it peaks already at $T \approx 25\,000 \text{ K}$ and also with much larger amplitude. Since the Si IV lines in the EB spectra of

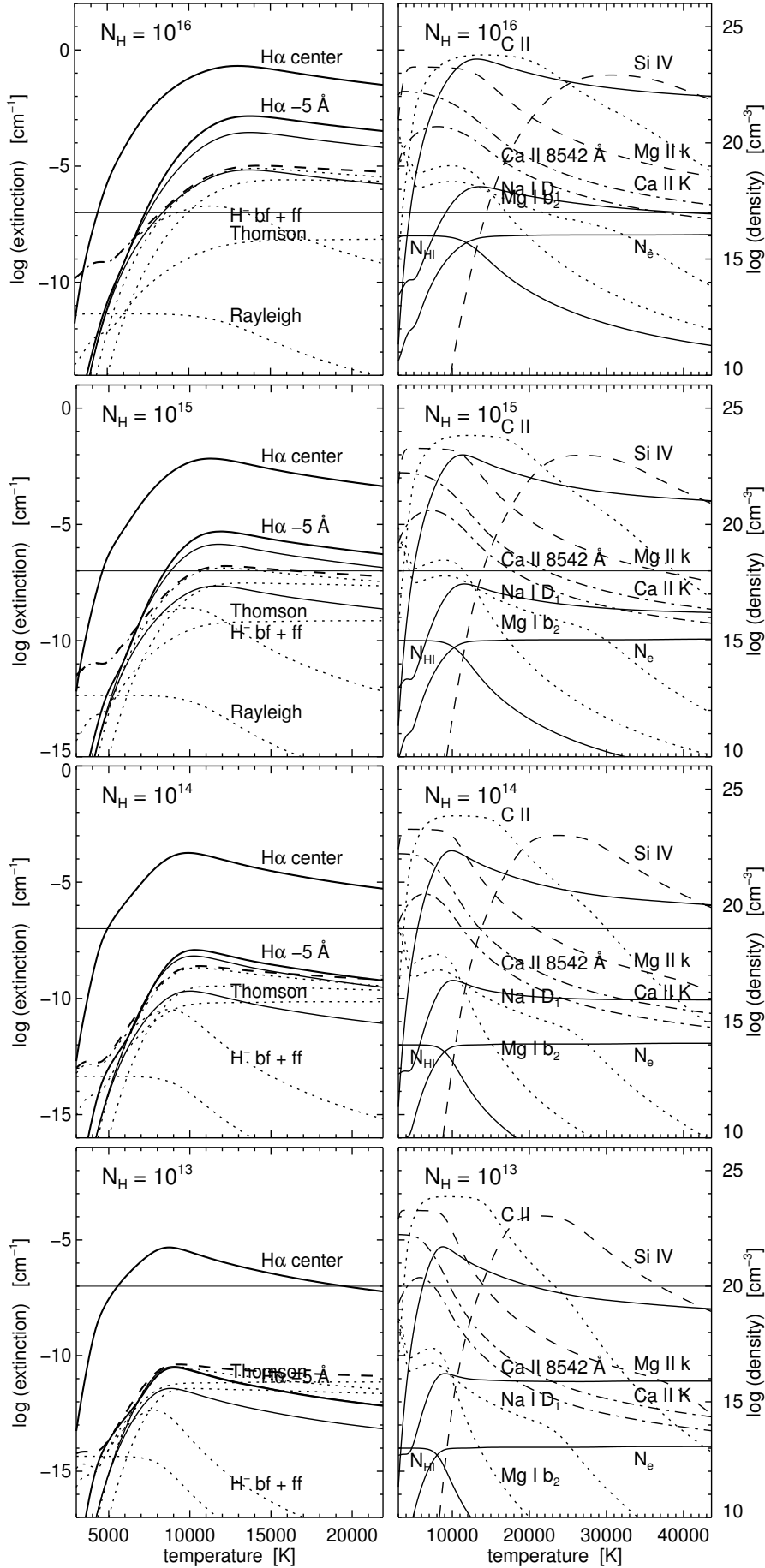


Fig. 5. Payne-style extinction comparisons for solar gas assuming LTE.

Top to bottom: total hydrogen density $N_H = 10^{16}, 10^{15}, 10^{14}, 10^{13} \text{ cm}^{-3}$, corresponding to heights 350, 615, 850 and 1150 km in ALC7 (Fig. 1). The logarithmic extinction scales along the y -axes shift upward between panels to compensate for the density decrease. The horizontal line at $y = -7$ marks optical thickness unity for a slab of 100 km geometrical thickness.

Left: the upper two solid curves show H α extinction at line center and in the wing at $\Delta\lambda = -5 \text{ \AA}$. The third solid curve is for $\Delta\lambda = -5 \text{ \AA}$ when using a Voigt instead of a Holtsmark distribution for linear Stark broadening. The lowest solid curve results when Stark broadening is neglected. The dashed curve is the total continuous extinction at the H α wavelength, made up by H $^-$ and H I bound-free and free-free transitions and by Thomson and Rayleigh scattering. The dotted curves show the separate continuum contributions (the top two for H I bound-free and free-free extinction are not labeled).

Right: the H α line-center extinction is shown again (uppermost solid curve) but over a doubled temperature range. It is compared with the line-center extinction of Mg II k (dashed), Ca II K and Ca II 8542 \AA (dot-dashed), Mg I b₂ and Na I D₁ (dotted), and the IRIS lines C II 1335.71 \AA (dotted) and Si IV 1393.75 \AA (dashed). The second solid curve is the total continuous extinction at 1700 \AA due to H $^-$, H I and continuous scattering. The two solid curves underneath show the competing neutral hydrogen density $N_{H I}$ and free electron density N_e on a comparable (but non-shifting) logarithmic scale specified along the y -axes at right.

Remarkable: at left the large effect of Stark broadening. At right the large H α extinction at high temperature.

Paper III reach only EB thickness $\tau \approx 1$ they may be formed on the rising branch and represent only $T \approx 15\,000 - 20\,000$ K.

3.2. H α extinction in LTE

Figure 5 shows extinction-versus-temperature diagrams that I wish to call “Cecilia Payne diagrams” although they are somewhat more elaborate than Payne’s curves. First, they show the LTE line extinction coefficient rather than the lower-level Saha-Boltzmann population by multiplying with the transition probability, the line profile, and the correction for stimulated emission (with $b_l = b_u = 1$ in Eq. 1). Second, they do not show curves for fixed electron pressure but for fixed total hydrogen density N_H (a parcel of solar gas in which the electron density varies with temperature according to the degree of ionization, especially of hydrogen).

N_H diminishes in ten-fold steps from top to bottom. In the ALC7 atmosphere these values correspond to heights 350, 615, 850, and 1150 km, respectively, sampling its upper photosphere and lower chromosphere (Fig. 1). The extinction scales along the lefthand y -axes shift accordingly.

The horizontal line at $y = -7$ corresponds to optical thickness unity along 100 km path length and schematically represents an EB in sideways viewing. Above this line a 100 km slab appears optically thick, below it optically thin.

This section discusses the first column. It shows comparisons between H α and the continuum. The various curves were computed using the formulae and tables in Gray (2005) for the element mix of Asplund et al. (2009). For H α linear Stark broadening was included using Gray’s equation (11.49) with the first approximation of Sutton (1978) for the Holtsmark distribution. The Saha equation was iterated for hydrogen, helium and the first two ionization stages of the abundant metals in order to obtain the free-electron density (shown at right).

The comparisons in the first column of Fig. 5 were prompted by the suggestion of Engvold & Maltby (1968) that the frequency redistribution which occurs in thermal electron scattering may cause the extraordinary EB moustaches by shifting H α line-core photons over large electron Dopplershift into the far H α wings. They stipulated that for this mechanism EBs must contain sufficient free electrons to offset the very small Thomson cross-section $\sigma_T = 6.65 \times 10^{-25} \text{ cm}^2$, quantifying that electron density $N_e = 10^{16} \text{ cm}^{-3}$ would be needed along a 1000-km line of sight through an EB to gain optical thickness of order unity. They suggested that this may be reached through hydrogen ionization in photospheric gas.

My initial enthusiasm for this mechanism (Sect. 6 of Rutten et al. 2013) was undone by the tests shown here, based on similar tests by J. Leenaarts (private communication). Neutral hydrogen extinction in the Paschen continuum takes over from H α extinction already below $T = 10\,000$ K, whereas Thomson scattering becomes the dominant continuum agent above $10\,000$ K only below hydrogen density $N_H \approx 10^{13} \text{ cm}^{-3}$ (bottom panel) with extinction below 10^{-10} cm^{-1} so that only one per thousand H α photons would be Thomson-scattered and Doppler-shifted in a 100-km EB slab. For more scattering the density must be higher, but then such a slab becomes opaque in the Paschen continuum.

In the ALC7 chromosphere the Paschen extinction drops significantly below the LTE value (dashed curve in the first panel of Fig. 1) due to photon losses in H α , but in HION this happens only in the green arches in Fig. 2, not in the shocks or the post-shock cool clouds. Therefore, the graphs in Fig. 5 suggest that EBs would be observed in the continuum well before Thomson

scattering would cause moustaches, making the suggestion of Engvold & Maltby (1968) incompatible with the observed EB transparency in the continuum.

In addition, other lines such as Ca II H and Ca II 8542 Å do show EB moustaches but less wide than H α (Hashimoto et al. 2010; private communication from R. Rezaei). For Thomson redistribution they should have similar extent since it acts the same for any line with similar core brightening below the fibril canopy.

Fortunately, the first column of Fig. 5 also suggests a more viable EB moustache mechanism: linear Stark broadening by electrons. In the second panel a 100-km slab is optically thick (extinction above 10^{-7} cm^{-1}) in the H α wing at $\Delta\lambda = -5$ Å from line center at all temperatures above 8000 K, while it becomes only barely opaque in the continuum at $T = 11\,000 - 15\,000$ K. This parameter domain may therefore explain EB visibility in the H α wing together with transparency in the continuum. However, it is essential that linear Stark broadening, a specific agent for Balmer lines, is included in the line formation computation since without it the H α wing has less extinction than the continuum. This is demonstrated by the lowest solid curve, which results from only accounting for radiation damping and Van der Waals broadening as done by Bello González et al. (2013).

The third solid curve from the top in each lefthand panel results when a Voigt function is used for the linear Stark broadening (as is done in the RH code) instead of the Holtsmark distribution. It lies slightly lower due to the slower Lorentzian $\sim (\Delta\lambda)^{-2}$ wing decay then Holtsmark $\sim (\Delta\lambda)^{-5/2}$ decay, which through area normalization produces profile cross-overs in the wings further out than $\Delta\lambda = -5$ Å.

The sampling wavelength $\Delta\lambda = -5$ Å of these comparisons was selected because the observed EB excess spectrum in Fig. 2 of Kitai (1983) suggests the start of optical thinness at about this wavelength for slab-like profile formation. In this EB the moustache extent was over 10 Å on each side of line center. Note that Ellerman (1917) specified bomb extents up to $\Delta\lambda = 15$ Å; so did Severny (1956) for moustaches.

Thus, linear Stark broadening seems a viable mechanism to transfer H α photons from the locally bright but obscured line core to escape in the outer wings and pass through overlying fibrils. Similarly to Thomson redistribution, it requires sufficient hydrogen ionization but it has much larger cross-section. I identify it therefore as a key agent producing bright extended H α moustaches and making the Balmer lines display the EB phenomenon so spectacularly.

3.3. LTE extinction of EB diagnostics

I now turn to the second column of Fig. 5. It compares the LTE extinction of H α with that of other EB diagnostics, again as function of temperature but over a larger temperature range. The different curves show LTE line-center extinction for the specified lines and the Balmer continuum extinction at 1700 Å, defined by their Boltzmann and Saha sensitivities to temperature and electron density. The electron and neutral hydrogen densities are overplotted in the bottom part of each panel, with axis scales at right.

The little plateau at the start of the N_e curve in the top panel, also evident in the 1700 Å curve, illustrates that ionization of abundant metal atoms provides the electrons for H α extinction in the low-temperature photosphere. At higher temperature the electrons come mostly from hydrogen. The cross-over point with 50% hydrogen ionization and $N_{H1} \approx N_e$ shifts from $T \approx 12\,000$ K to $T \approx 8\,000$ K from top to bottom. The curves and their cross-

over temperature values change correspondingly between panels, but not drastically.

In the lefthand column the second panel suggested $\log(N_H) \approx 15$ and $T \gtrsim 10\,000$ K as viable target parameters to obtain H α wing visibility combined with continuum transparency for the 100-km slab. The righthand column permits such LTE visibility estimation also for the other EB diagnostics. I discuss them one by one.

H α . The uppermost solid curve in each panel is again the H α line-center extinction, identical to the corresponding curves at left. The most striking feature in these graphs is the discordant behavior of H α due to its combination of exceedingly large elemental abundance and exceedingly large excitation energy. In each graph the H α line-center extinction shows a steep rise with temperature due to its Boltzmann population factor, followed by a decline due to hydrogen ionization which is considerably tempered by the ever-increasing relative excitation. At low temperature H α has no significant extinction whatsoever, but above $T \approx 8000$ K H α becomes much stronger than Ca II K, the reverse of their photospheric ratio, and H α even beats Mg II k significantly above $T = 12\,000$ K. This extraordinary strength may actually yet increase through the much slower decay for CE ionization (Fig. 4) combined with Boltzmann excitation forcing by Ly α .

A numerical fit of the locations of the peaks of the H α extinction curves, which are defined by the sensitivities of the Boltzmann, Saha, profile shape and induced emission terms in Eq. 1, shows that these obey:

$$\log(n_2/N_H) = 0.683 \log(N_H) - 14.8, \quad (5)$$

which provides a quick estimate of the maximum extinction that H α can reach in dynamical situations with onset LTE validity.

The H α and Ca II 8542 Å curves cross at $T \approx 7\,000 - 8\,000$ K. The 100-km slab is optically thick at this curve cross-over in all panels, conform the invisibility of EBs at the centers of these lines from obscuration by the fibrillar canopy (Paper I).

H α 's special combination of very large high-temperature extinction with very small low-temperature extinction also implies that a high-temperature slab embedded in cool gas can display large H α wing emissivity within a transparent environment, without shielding along lines of sight as C and B in Fig. 2. Fig. 5 suggests that cool surrounding gas will not have any H α opacity. The fractional population curve (dashed) in the first panel of Fig. 1 shows that in the ALC7 atmosphere the H α opacity is indeed negligible between the deep photosphere and the chromospheric plateau.

Close to an EB absorption of Ly α photons from the EB itself boosts the surrounding $n = 2$ population as demonstrated in Sect. 2.4, but the extent of such halos is small and they occur only in the H α core in which the halo is invisible anyhow from obscuration by overlying fibrils. In the outer H α wings surrounding cool gas lacks moustache opacity from shortage of free electrons for Stark broadening. The therefore unmolested H α -moustache sharpness permits, at sufficiently high angular resolution, to resolve very fine substructure within EBs, as observed in Hashimoto et al. (2010) and Paper I.

Also, the hotter EB top observed along line of sight A retains large H α emissivity thanks to the slow extinction decline for increasing temperature.

Balmer continuum. The second solid curve is the continuous extinction due to hydrogen and continuous (Thomson and

Rayleigh) scattering at 1700 Å. In the top panels of Fig. 5 these curves mimic the H α curve because both are set by the hydrogen $n = 2$ population. In the lower panels Thomson extinction flattens the 1700 Å curves, similarly to the dashed 6563 Å continuum curves (with Paschen instead of Balmer extinction) in the lefthand column. The 1700 Å curve peaks just below the $\tau = 1$ line for the 100-km slab in the second panel; thickness requires a wider slab or larger density.

Below 10 000 K the 1700 Å extinction is dominated by bound-free Si I and Fe I edges, but at higher temperature the main agent is the Balmer continuum. This is already evident in the classic LTE continuum extinction diagrams (in German) in Figs. I–XV of Vitense (1951), the third landmark thesis by a heroine of astrophysics emulated here. They have been redrawn (in English and with better graphics) in Figs. 3–12A–O of Novotny (1973). I do not include the cool-gas Si I and Fe I contributions here because LTE would give severe overestimation also for surrounding gas. They are diminished through photoionization already in the upper photosphere of 1D standard models (Vernazza et al. 1981) and are further depleted near hot EBs through irradiation by these.

The ultraviolet continua are all strongly resonant-scattering, as evident from the superb formation diagrams in Fig. 36 of Vernazza et al. (1981). In their VALIIC model the Eddington-Barbier $\tau = 1$ heights around 1700 Å range over 300–500 km, but most photons are thermally created in the deep photosphere and then scatter out with a $S \approx J$ decline which, opposite to the line scattering in Fig. 1, has $J > B$ from the combination of temperature gradient setting by optical photon losses, deep formation, large Wien temperature sensitivity, and the gradient sensitivity of the Lambda operator (Chapt. 4 of RTSA). A deeply located temperature increase boosts J and the emergent continuum intensity across the ultraviolet while an increase near $\tau = 1$ does not. Even along line of sight C in Fig. 2 the bright foot of an EB so has ultraviolet visibility, be it diffuse from surround scattering by the remaining Si and Fe atoms and in the Balmer continuum boosted by Ly α irradiation.

Large depth provides the density needed for noticeable Balmer-continuum brightening (Fig. 5). In addition, since EBs are bi-modal jets, compression at the lower shock likely enhances the local Balmer-continuum production.

The 1700 Å–H α -wing comparisons in Fig. 6 of Paper II, Fig. 4 of Rutten et al. (2013), and Figs. 2, 6, 9 of Paper III indeed suggest, even at the low AIA resolution, that EBs appear more extended in the 1700 Å images than in the H α -wing images, that the 1700 Å images favor EB feet, and that these show the largest blurring. The IRIS spectra in Paper IV indeed show EB brightening in the 1400 Å continuum.

Ca II lines. Ca II K and Ca II 8542 Å have similar curves in Fig. 5 except for the Boltzmann sensitivity of the latter. In both lines the slab is thick for the target parameters, but overlying cooler fibrils are yet thicker so that only wing brightenings result, at smaller moustache extent than for H α since these lines suffer no Stark broadening. This is also conform observations (Paper II for Ca II 8542 Å, Hashimoto et al. 2010 for Ca II H).

At temperatures above their cross-overs in Fig. 5 H α and Ca II 8542 Å have opposite temperature sensitivity, implying that the Ca II 8542 Å wings favor cooler EB feet, the H α wings hotter EB tops. This is seen in Fig. 3 of Paper II. In addition, the downward-directed part of a bi-modal EB jet favors blue-wing emission, also evident in that figure. Furthermore, the larger

Ca II extinction at lower temperature implies scattering in surrounding cooler gas causing defocus, also evident in that figure. For Ca II H diffuse EB halos were reported by Matsumoto et al. (2008).

Na I D₁ and Mg I b₂. These lines have cross-over extinction curves in Fig. 5 (dotted), with Mg I b₂ stronger below $T \approx 10\,000$ K. Both curves decay above 10 000 K from increasing ionization, but less steep for Na I D₁ due to the high Na II ionization energy (47.3 eV, highest after Li and He. The initial steep declines are also from increasing ionization, but over 4000–10 000 K ionization diminishes due to the increasing electron density.

In the $N_H = 10^{15}$ panel the 100-km slab reaches about $\tau \approx 1$ in both line centers near $T \approx 10\,000$ K, but remains less opaque than in gas with $T \approx 4000$ K or less around EBs. Photon suction as in ALC7 enhances cool-gas extinction beyond the LTE estimate. Obscuration along lines of sight as C and B in Fig. 2 is therefore probable. EBs are indeed not observed in the cores of these lines, in exceptional cases only in the wings of Mg I b₂ (Paper IV). For this line ultraviolet Mg I overionization may offset the suction increase, as in Fig. 1 (compare the b_l curves of the two lines).

IRIS lines. For the ultraviolet IRIS lines the second panel predicts enormous slab opacity in the C II and Mg II k lines for $T \approx 10\,000$ K, but invisibility for the Si IV lines which actually showed EBs “thin” ($\tau \approx 1$) in Paper III. That value is reached at $T \approx 15\,000$ K, towards the Si IV curve peaks around $T = 25\,000$ K as in Fig. 4. It does so in all panels since the leftward shifts of the Si IV curve for lower electron density are offset by the downward shifts for lower gas density (upward y -axis shifts) in sampling the steep curve increases. The assumption of LTE ionization is least likely for this diagnostic, but departures shift the curves to higher temperature as in Fig. 4; $T \approx 15\,000$ K represents a minimum estimate.

One might expect that such high temperatures are only reached in EB tops, but the IRIS spectra in Paper III also show enhanced-intensity redshifted Si IV profiles with the slitjaw images confirming that these come from lower EB parts. The blueshifted profiles from the upper parts are brighter and wider, but nevertheless also EB feet show up.

Surrounding gas can also affect the ultraviolet EB signatures. Most spectra in Paper III contain absorption blends: Mn I blends on Mg II & k without Dopplershifts, Fe II and Ti II blends on the Si IV and C II lines with 10 km s^{-1} blueshifts. The first were attributed to undisturbed upper-photosphere gas along lines of sight as C in Fig. 2, the latter to upper-clapotisphere gas containing shocks along lines of sight as B. Lines of sight as A then sample hot EB tops without such blends.

These blends and their small Dopplershifts, observed not only in EBs but also in FAFs (Paper III), support the conclusion of Peter et al. (2014) that IBs occur at large depths. For EBs this was already established in Paper I: they have their feet in the low photosphere. Comparison of the IRIS spectra and cutout images in Paper III shows that profiles with deep Mn I blends correspond to lower-part samplings with the largest 1700 Å (EBs) or 1600 Å (FAFs) halos, suggesting photospheric formation even within the narrow Judge sense adopted in Sect. 2.6.

EBs appear as sharp in the Si IV lines as in H α moustaches: without obscuration by overlying fibrils and without defocusing by surrounding gas. The nominal continuum at 1400 Å has Balmer brightening in EBs with scattering halos comparable to

1700 Å, but the Si IV lines from EBs are much brighter and dominate the IRIS 1400 Å slitjaw passband (Paper III). The lines from a deep EB foot suffer some surround scattering as observed in the blurred 1700 Å signature, either in the Si I edge that contributes most continuous opacity at 1400 Å in cool gas but is depleted by irradiation from the EB or in the Balmer edge boosted by Ly α irradiation. However, even if a sizable fraction of the Si IV emission from an EB foot suffers such surround scattering, this undergoes complete redistribution over the edge with most re-emission near its threshold. It causes only gray attenuation of the lines, not affecting their relative profile shape or image sharpness. There is indeed good size and morphology likeness between the 1400 Å and H α -wing images in Figs. 2, 6 and 9 of Paper III.

3.4. EB density and temperature estimation

This section discusses how the graphs in Fig. 5 constrain the density and temperature parameter space of EB onsets assuming the LTE recipes of Sect. 2.

The second column of Fig. 5 shows only line-center extinctions to minimize figure clutter. However, as for H α in the left-hand column, not the line-center but the wing extinction should be estimated for those diagnostics that only show EBs in their wings – all of them except the Si IV lines and the 1700 Å continuum. All curves except these two should therefore be shifted downward over 1–2 log units. At 10 000 K Na I D₁ and Mg I b₂ then become weaker than the 1700 Å continuum, in agreement with the actual EB visibilities.

However, these are not the only shifts to be applied. An obvious one is to shift the $y = -7$ line vertically by selecting different slab thickness. My arbitrary choice of 100 km was inspired by typical diameters of network MCs. A thinner slab requires higher density to reach $\tau = 1$.

Another shifting agent is extinction memory of hot prior moments, as the Balmer lines and the Balmer continuum possess in HION shock aftermaths. If hot and dense EB onsets are also followed by cooler, more tenuous aftermaths then similar delays in population adjustment may occur. Such memory then implies leftward shifts of the H α and 1700 Å extinction curves, retaining the extinction of the hotter moment in the past into the cooler present. Similar memory shifts may also occur for the Si IV and C II lines.

An example scenario is that EB tops heat to 20 000 K in their onset, gain $\tau \approx 1$ opacity (and corresponding emissivity) in the Si IV lines, and retain this as well as high Balmer line-wing and continuum emissivity during subsequent cooling.

Furthermore, EBs are not homogeneous slabs but appear hotter higher up (Paper III). The curve patterns in Fig. 5 illustrate that the optical lines except H α favor cooler and denser gas than the IRIS lines. The former are more likely to sample the lower parts of an EB as along lines of sight C to B in Fig. 2, the latter the hotter and more tenuous upper parts along lines of sight B to A. H α is special in showing the full EB extent.

The upshot is that Fig. 5 does not define a single [temperature, density] locus to pinpoint all EB visibilities, but with these various curve-shifting options it does suggest the domain where they originate: hydrogen density around 10^{15} cm^{-3} , time-dependent temperatures in the 10 000–20 000 K range.

4. Discussion

The suggested EB onset temperature domain is quite hot, but where the LTE recipes become invalid the temperatures required to explain the actual EB visibilities, especially in the Si IV lines, must be substantially higher, even nearing the CE limits.

The suggested domain is significantly hotter than the relative heating obtained by Archontis & Hood (2009) in their EB simulation. However, more recent MHD simulations of comparable reconnection phenomena show larger heating (Archontis & Hansteen 2014; Lee et al. 2015), likely through magnetosonic wave excitation and dissipation (Longcope & Priest 2007). It is beyond the observational nature of this paper to discuss or suggest how EBs may magnetically heat dense photospheric gas to the temperatures required for their visibilities, but clearly EBs represent an intriguing challenge for such endeavors.

The suggested domain is also very dense, but large densities may indeed occur in reconnection events within the photosphere, especially at shocks from the downward-directed jet in the observed bi-modal pattern.

A final speculation concerns the line source functions. All lines studied here are resonant-scattering in the ALC7 chromosphere (Fig. 1), even H α , and so are the ultraviolet continua through bound-free scattering. However, in EBs, especially in their later cooling phases, the detour contribution in the third term in Eq. 2 may outweigh the second through recombination paths. A tell-tale is emission in the double Mg II triplet line between Mg II h & k, of which examples are shown in Paper III. The high ionization energy of Mg III (80 eV, highest after Li and Be) makes this likely by making Mg III the population reservoir over 10 000–40 000 K (Fig. 4), enhancing recombination from it.

5. Conclusion

The extinction estimates in Fig. 5 suggest that EBs have hydrogen densities of about 10^{15} cm^{-3} and temperatures in the 10 000–20 000 K range, much hotter than all NLTE modeling of EBs so far but far cooler than CE modeling would suggest.

Of the various EB diagnostics H α is the most outstanding thanks to its electron-sensitive broadening, huge elemental abundance, and large excitation energy. The latter two combine into exceedingly large high-temperature extinction; the Stark broadening produces observable moustaches by shifting the corresponding hot-gas emissivity from the fibril-observed core to the extended line wings. The large excitation energy also causes extinction and emissivity memory for hotter moments through retarded recombination balancing. It also causes H α -wing transparency of cooler surrounding and overlying gas, permitting unobstructed EB viewing.

The AIA 1600 and 1700 Å channels are also good EB diagnostics because at high temperature they are dominated by the Balmer continuum which shares the H α properties – except Stark broadening, but they do not need that because overlying fibrils (as the pink one in Fig. 2) are transparent at these wavelengths. However, this imaging is defocused by bound-free scattering in surrounding gas.

Clean EB imaging as in H α moustaches is also furnished by the Si IV lines in which the overlying fibril canopy is also transparent while the Balmer-continuum irradiation by EB feet burns an opacity hole around them and bound-free surround scattering causes no defocus.

How to proceed? The present state of EB research resembles Ca II K $_{2V}$ grain research two decades ago. EBs are minuscule rare brightenings of the outer H α wings that are hard to explain,

as evident from the large but confused literature (Rutten et al. 2013). K $_{2V}$ grains are minuscule (but ubiquitous) brightenings of the inner Ca II K wings that were then also hard to explain, as evident from the large but confused literature at the time (Rutten & Uitenbroek 1991). The K $_{2V}$ puzzle was solved with the data-driven simulation of Carlsson & Stein (1997); the clincher was that the observed spectral grain evolution pattern is so specific that its precise reproduction (on the cover of Carlsson 1994) implied undeniable simulation verification.

It seems obvious that the next step in EB research must be similar reproduction of the rich set of EB visibilities in diverse diagnostics through numerical MHD simulation with detailed spectrum synthesis. The observations in Papers I–IV provide sufficient constraints for undeniable simulation verification.

I do not suggest LTE as a viable approach for such effort. I have used the assumption of Saha-Boltzmann lower-level populations here to gauge the ballpark of EB extinction values in the initial hot and dense EB onsets. These may be close to LTE (Sect. 2.3) or yet higher (Sect. 2.2), but the evaluation of the aftermaths must be non-E to track the level populations during the further evolution.

While non-E 3D simulation including detailed non-E 3D radiative transfer remains too resource-demanding, a shortcut simplification for single-snapshot H α synthesis is to maintain or slowly decay fractional hydrogen populations after their peak, or simply set the $n=2$ population with Eq. 5.

Observationally, EBs present a perfect target for solar telescopes to verify promised angular resolution. The clean viewing of EB H α moustaches implies rendering of detail down to kilometer scales, far below the photon path lengths that affect other optical diagnostics. In addition, the intrinsic moustache contrast is high so that resolving fine structure is feasible at moderate Strehl ratio. At good seeing the spatial moustache resolution is therefore limited only by the telescope aperture and quality.

The 25 km resolution at H α and Strehl above 0.6 promised for the Daniel K. Inouye Solar Telescope are commensurate with simulation resolutions. Thus, EBs may become the first solar reconnection phenomenon diagnosed and understood in full detail.

The time seems also ripe to exploit the full-time full-disk sampling of EB occurrences which AIA delivers in its 1700 Å channel to use EBs as pin-pointers of photospheric strong-field reconnection events for charting active-region field reconfiguration. This is likely yet more fruitful for FAFs sampled likewise by AIA's 1600 Å channel. They are EB siblings with the added interest that they affect the higher solar atmosphere and so provide direct lower boundary constraints to coronal field evolution.

Finally, the onset-LTE recipes given above may explain extraordinary H α visibility in other sudden heating events and their aftermaths. They then similarly invalidate SE modeling of such phenomena.

Acknowledgements. I am much indebted to C. Zwaan (1928–1999) who often suggested EB line formation as research topic. The didactic nature of this paper bears his stamp. H. Uitenbroek provided the newest version of RH. Comments from J. Leenaarts and the referee improved the presentation. CHIANTI is a project of George Mason University, the University of Michigan and the University of Cambridge. As always, I made much use of NASA's ADS and the SolarSoft library.

References

- Archontis, V. & Hansteen, V. 2014, ApJL, 788, L2 [ADS](#)
- Archontis, V. & Hood, A. W. 2009, A&A, 508, 1469 [ADS](#)
- Asplund, M., Grevesse, N., Sauval, A. J., & Scott, P. 2009, ARA&A, 47, 481 [ADS](#)

- Athay, R. G. & Thomas, R. N. 1961, *Physics of the solar chromosphere* [ADS](#)
- Avrett, E. H. 1965, *SAO Special Report*, 174, 101 [ADS](#)
- Avrett, E. H. & Loeser, R. 2008, *ApJS*, 175, 229 [ADS](#)
- Bello González, N., Danilovic, S., & Kneer, F. 2013, *A&A*, 557, A102 [ADS](#)
- Berlicki, A. & Heinzel, P. 2014, *A&A*, 567, A110 [ADS](#)
- Berlicki, A., Heinzel, P., & Avrett, E. H. 2010, *MmSAI*, 81, 646 [ADS](#)
- Bernasconi, P. N., Rust, D. M., Georgoulis, M. K., & Labonte, B. J. 2002, *SoPh*, 209, 119 [ADS](#)
- Bruls, J. H. M. J., Rutten, R. J., & Shchukina, N. G. 1992, *A&A*, 265, 237 [ADS](#)
- Bruzek, A. & Durrant, C. J., eds. 1977, *Astrophysics and Space Science Library*, Vol. 69, *Illustrated glossary for solar and solar-terrestrial physics* [ADS](#)
- Carlsson, M., ed. 1994, *Chromospheric dynamics* [ADS](#)
- Carlsson, M. & Leenaarts, J. 2012, *A&A*, 539, A39 [ADS](#)
- Carlsson, M. & Stein, R. F. 1994, in *Chromospheric Dynamics*, ed. M. Carlsson, 47 [ADS](#)
- Carlsson, M. & Stein, R. F. 1997, *ApJ*, 481, 500 [ADS](#)
- Carlsson, M. & Stein, R. F. 2002, *ApJ*, 572, 626 [ADS](#)
- De Pontieu, B., Title, A. M., Lemen, J. R., et al. 2014, *SoPh*, 289, 2733 [ADS](#)
- Dere, K. P., Landi, E., Mason, H. E., Monsignori Fossi, B. C., & Young, P. R. 1997, *A&A Suppl.*, 125, 149 [ADS](#)
- Ellerman, F. 1917, *ApJ*, 46, 298 [ADS](#)
- Engvold, O. & Maltby, P. 1968, in *Mass Motions in Solar Flares and Related Phenomena*, ed. Y. Oehman, 109 [ADS](#)
- Fontenla, J. M., Curdt, W., Haberreiter, M., Harder, J., & Tian, H. 2009, *ApJ*, 707, 482 [ADS](#)
- Golding, T. P., Carlsson, M., & Leenaarts, J. 2014, *ApJ*, 784, 30 [ADS](#)
- Gray, D. F. 2005, *The Observation and Analysis of Stellar Photospheres* (3rd edition, Cambridge University Press) [ADS](#)
- Hashimoto, Y., Kitai, R., Ichimoto, K., et al. 2010, *PASJ*, 62, 879 [ADS](#)
- Hubeny, I. & Mihalas, D. 2014, *Theory of Stellar Atmospheres* [ADS](#)
- Hummer, D. G. & Rybicki, G. 1967, in *Methods in Computational Physics* Vol. 7, *Astrophysics*, ed. B. Alder, S. Fernbach, & M. Rotenberg (New York: Academic Press), 53–127
- Isobe, H., Tripathi, D., & Archontis, V. 2007, *ApJL*, 657, L53 [ADS](#)
- Jefferies, J. T. 1968, *Spectral line formation* [ADS](#)
- Jordan, C. 1969, *MNRAS*, 142, 501 [ADS](#)
- Kitai, R. 1983, *SoPh*, 87, 135 [ADS](#)
- Kneer, F. 1980, *A&A*, 87, 229 [ADS](#)
- Kurucz, R. L. 2009, in *American Institute of Physics Conference Series*, Vol. 1171, *American Institute of Physics Conference Series*, ed. I. Hubeny, J. M. Stone, K. MacGregor, & K. Werner, 43–51 [ADS](#)
- Landi, E., Young, P. R., Dere, K. P., Del Zanna, G., & Mason, H. E. 2013, *ApJ*, 763, 86 [ADS](#)
- Lee, E. J., Archontis, V., & Hood, A. W. 2015, *ApJL*, 798, L10 [ADS](#)
- Leenaarts, J., Carlsson, M., Hansteen, V., & Rutten, R. J. 2007, *A&A*, 473, 625 [ADS](#)
- Leenaarts, J., Carlsson, M., & Rouppe van der Voort, L. 2012, *ApJ*, 749, 136 [ADS](#)
- Leenaarts, J., Carlsson, M., & Rouppe van der Voort, L. 2015, *ApJ*, 802, 136 [ADS](#)
- Leenaarts, J., Pereira, T. M. D., Carlsson, M., Uitenbroek, H., & De Pontieu, B. 2013, *ApJ*, 772, 89 [ADS](#)
- Leenaarts, J., Rutten, R. J., Sütterlin, P., Carlsson, M., & Uitenbroek, H. 2006, *A&A*, 449, 1209 [ADS](#)
- Lemen, J. R., Title, A. M., Akin, D. J., et al. 2012, *SoPh*, 275, 17 [ADS](#)
- Lockyer, J. N. 1868, *Proceedings of the Royal Society of London Series I*, 17, 131 [ADS](#)
- Longcope, D. W. & Priest, E. R. 2007, *Physics of Plasmas*, 14, 122905 [ADS](#)
- Matsumoto, T., Kitai, R., Shibata, K., et al. 2008, *PASJ*, 60, 577 [ADS](#)
- McMath, R. R., Mohler, O. C., & Dodson, H. W. 1960, *Proceedings of the National Academy of Science*, 46, 165 [ADS](#)
- Mihalas, D. 1967, in *Methods in Computational Physics* Vol. 7, *Astrophysics*, ed. B. Alder, S. Fernbach, & M. Rotenberg (New York: Academic Press), 1–52
- Nelson, C. J., Shelyag, S., Mathioudakis, M., et al. 2013, *ApJ*, 779, 125 [ADS](#)
- Novotny, E. 1973, *Introduction to stellar atmospheres and interiors* (Oxford University Press) [ADS](#)
- Pariat, E., Aulanier, G., Schmieder, B., et al. 2004, *ApJ*, 614, 1099 [ADS](#)
- Pariat, E., Masson, S., & Aulanier, G. 2009, *ApJ*, 701, 1911 [ADS](#)
- Payne, C. H. 1924, *Harvard College Observatory Circular*, 256, 1 [ADS](#)
- Payne, C. H. 1925, *PhD thesis*, Radcliffe College [ADS](#)
- Pesnell, W. D., Thompson, B. J., & Chamberlin, P. C. 2012, *SoPh*, 275, 3 [ADS](#)
- Peter, H., Tian, H., Curdt, W., et al. 2014, *Science*, 346, 1255726 [ADS](#)
- Rutten, R. J. 1995, in *ESA Special Publication*, Vol. 376, *Helioseismology*, 151 [ADS](#)
- Rutten, R. J. 2003, *Radiative Transfer in Stellar Atmospheres* [ADS](#) (RTSA)
- Rutten, R. J., Rouppe van der Voort, L. H. M., & Vissers, G. J. M. 2015, *ApJ*, 808, 133 [ADS](#) (Paper IV)
- Rutten, R. J. & Uitenbroek, H. 1991, *SoPh*, 134, 15 [ADS](#)
- Rutten, R. J. & Uitenbroek, H. 2012, *A&A*, 540, A86 [ADS](#)
- Rutten, R. J., Vissers, G. J. M., Rouppe van der Voort, L. H. M., Sütterlin, P., & Vitas, N. 2013, *Journal of Physics Conference Series*, 440, 012007 [ADS](#)
- Rybicki, G. B. & Lightman, A. P. 1979, *Radiative processes in astrophysics* [ADS](#)
- Sánchez Almeida, J. 1992, *SoPh*, 137, 1 [ADS](#)
- Sánchez Almeida, J. 1997, *ApJ*, 491, 993 [ADS](#)
- Scharmer, G. B., Bjelksjo, K., Korhonen, T. K., Lindberg, B., & Petterson, B. 2003, in *Society of Photo-Optical Instrumentation Engineers (SPIE) Conference Series*, Vol. 4853, *Innovative Telescopes and Instrumentation for Solar Astrophysics*, ed. S. L. Keil & S. V. Avakyan, 341–350 [ADS](#)
- Scharmer, G. B., Narayan, G., Hillberg, T., et al. 2008, *ApJL*, 689, L69 [ADS](#)
- Severny, A. B. 1956, *The Observatory*, 76, 241 [ADS](#)
- Shimizu, T., Shine, R. A., Title, A. M., Tarbell, T. D., & Frank, Z. 2002, *ApJ*, 574, 1074 [ADS](#)
- Shine, R. A., Milkey, R. W., & Mihalas, D. 1975, *ApJ*, 199, 724 [ADS](#)
- Sutton, K. 1978, *J. Quant. Spec. Radiat. Transf.*, 20, 333 [ADS](#)
- Thomas, R. N. 1957, *ApJ*, 125, 260 [ADS](#)
- Uitenbroek, H. 2001, *ApJ*, 557, 389 [ADS](#)
- Vernazza, J. E., Avrett, E. H., & Loeser, R. 1981, *ApJS*, 45, 635 [ADS](#)
- Vissers, G. J. M., Rouppe van der Voort, L. H. M., & Rutten, R. J. 2013, *ApJ*, 774, 32 [ADS](#) (Paper II)
- Vissers, G. J. M., Rouppe van der Voort, L. H. M., Rutten, R. J., Carlsson, M., & De Pontieu, B. 2015, *ApJ*, 812, 11 [ADS](#) (Paper III)
- Vitense, E. 1951, *Z. Astrophys.*, 28, 81 [ADS](#)
- Watanabe, H., Vissers, G., Kitai, R., Rouppe van der Voort, L., & Rutten, R. J. 2011, *ApJ*, 736, 71 [ADS](#) (Paper I)
- Wedemeyer-Böhm, S. & Carlsson, M. 2011, *A&A*, 528, A1 [ADS](#)
- Wittmann, A. 1974, *SoPh*, 35, 11 [ADS](#)